atmosphere

MDPI

Article

Distinguishing Convective-Transition Moisture-Temperature Relationships with a Constellation of Polarimetric Radio Occultation Observations in and near Convection

F. Joseph Turk [1,*], Ramon Padullés [2,3], David D. Morabito [1], Todd Emmenegger [4] and J. David Neelin [4]

[1] Jet Propulsion Laboratory, California Institute of Technology, Pasadena, CA 91109, USA; david.d.morabito@jpl.nasa.gov
[2] Institute of Space Sciences (ICE, CSIC), 08193 Cerdanyola del Vallès, Spain; padulles@ice.csic.es
[3] Institute for Space Studies of Catalonia (IEEC), 08034 Barcelona, Spain
[4] Department of Atmospheric & Oceanic Sciences, University of California, Los Angeles, CA 90095, USA; temmen@atmos.ucla.edu (T.E.); neelin@atmos.ucla.edu (J.D.N.)
* Correspondence: jturk@jpl.nasa.gov

Abstract: Convective transition statistics serve as diagnostics for the parameterization of convection in climate and weather forecast models by characterizing the dependence of convection on the humidity-temperature environment. The observed strong pickup of precipitation as a function of layer-averaged water vapor and temperature is captured in models with varying accuracy. For independent observational verification, a low-Earth orbiting satellite constellation of Global Navigation Satellite System (GNSS) polarimetric radio occultation (PRO) measurements would be spaced such that adjacent RO would capture different profiles within and immediately adjacent to convection. Here, the number of profile observations needed to distinguish between convective transition relations by different tropospheric temperature ranges is determined, over different tropical oceanic basins. To obtain these, orbit simulations were performed by flying different satellite constellations over global precipitation from the Global Precipitation Measurement (GPM) mission, varying the numbers of satellites, orbit altitude, and inclination. A 45-degree orbit inclination was found to be a good tradeoff between maximizing the number of observations collected per day, and the desired 50–150-km spacing between individual RO ray paths. Assuming a set of reasonable assumptions for net data yield, three tropospheric temperatures can be distinguished by 1 K with a six-month on-orbit duration from a constellation of at least three satellites.

Keywords: convection; precipitation; moisture; climate; GPM; GNSS; GPS; satellite; occultation

check for updates

Citation: Turk, F.J.; Padullés, R.; Morabito, D.D.; Emmenegger, T.; Neelin, J.D. Distinguishing Convective-Transition Moisture-Temperature Relationships with a Constellation of Polarimetric Radio Occultation Observations in and near Convection. *Atmosphere* **2022**, *13*, 259. https://doi.org/10.3390/atmos13020259

Academic Editors: Zhen Zeng and Richard Anthes

Received: 24 December 2021
Accepted: 29 January 2022
Published: 2 February 2022

Publisher's Note: MDPI stays neutral with regard to jurisdictional claims in published maps and institutional affiliations.

Copyright: © 2022 by the authors. Licensee MDPI, Basel, Switzerland. This article is an open access article distributed under the terms and conditions of the Creative Commons Attribution (CC BY) license (https://creativecommons.org/licenses/by/4.0/).

1. Introduction

Despite the ongoing improvement in the resolution of weather and climate models [1], convective parameterization remains a major contributor to the uncertainty of future projections of global precipitation. Convective parameterization is a procedure whereby the joint effects of many (smaller scale) convective clouds are specified in terms of the larger-scale environmental conditions, such as temperature and moisture. While some recent climate models were insufficiently sensitive to lower free-tropospheric moisture, more realistic representations of entrainment and mixing [2] tend to improve this [3,4]. Some models of the Coupled Model Intercomparison Project Phase 6 (CMIP6) ensemble can be overly sensitive to free tropospheric moisture [5]. Convective transition statistics (discussed in Section 2) provide a useful set of simple statistical relationships for model diagnostics compared to observations [6,7]. The analysis in [6] compared pairs of models that differed primarily in their moist convective parameterization schemes and concluded that the convection transition statistics can distinguish among different parameterization assumptions, which has implications for model performance from short-term numerical weather prediction

(NWP) weather forecasts to future climate scenarios. To date, observations with vertically resolved moisture have been carried out with ground-based stations [8] with limited spatial coverage. A dense space-based profiling capability in the tropical latitudes would offer the opportunity to perform convective transition analysis globally, to address key questions such as:

1. Is high lower free tropospheric moisture a prerequisite to heavy deep-convective precipitation events, and to which levels does the convection appear to be the most sensitive?
2. Are there substantial differences in the above relationships amongst different oceanic basins, where forcing effects such as surface wind convergence may be different, or between tropical land and ocean regions?
3. How closely does the suite of current climate models replicate the observed convective transition statistics?

Recent years have witnessed rapid miniaturization of millimeter (mm)-wave and sub-mm wave electronics and hardware including passive microwave (MW) sounders [9], and Ka- and W-band radars [10,11], suitable for constellations of small low Earth-orbiting (LEO) satellite atmospheric science investigations [12,13]. The Global Navigation Satellite System (GNSS) radio occultation (RO) measurement has unique advantages when deployed in a small satellite constellation. Rather than sense clouds by backscatter or thermal emission, the RO measurement is a precise-time measurement technique providing the environmental temperature, pressure, and moisture (T, p, q, respectively) structures at a fine-scale vertical resolution (~100 m to 1 km, depending on height) necessary to separate water vapor within different vertical layers. When the GNSS signal propagates through a region of large enough aspherical hydrometeors such as heavy precipitation, a propagation differential (horizontal minus vertical, or H-V) phase shift is induced, denoted as $\Delta\varphi = \varphi_H - \varphi_V$ [14], measurable with a polarimetric RO (PRO) receiver with dual orthogonal (H/V) polarimetric receive antenna (in this manuscript, the acronym RO refers to the radio occultation measurement, and the acronym PRO is used to refer specifically to an RO with polarimetric receive capability).

The Radio Occultations through the Heavy Precipitation (ROHP) demonstration receiver onboard the Spanish PAZ satellite (deployed in February 2018) has successfully demonstrated the PRO concept [15]. Essentially, $\Delta\varphi$ complements the typical RO processing, providing direct complementary indication of heavy precipitation at each profile level. That is, the moisture profile and its corresponding precipitation detection profile are provided directly by the same observation. The attenuation by clouds and precipitation at GNSS frequencies is insignificant, providing a unique capability of PRO to probe the moisture structure through extreme precipitation weather systems and in the nearby environment with similar accuracy, during all stages of cloud development.

Despite its fairly coarse along-ray resolution of 200 km, the "across-ray" resolution of an RO is fine scale (~1-km). Coupled with its innate fine vertical resolution, an RO measurement is an inherently fine-scale measurement in two of the three spatial dimensions (Figure 1). In this graphical depiction, an on-Earth projection of the lowest 200-km segment of the RO ray paths (corresponding to the low levels where the majority of the water vapor is present) is shown intersecting precipitation, centered upon the corresponding on-Earth tangent point. We note that this is an idealized representation of actual conditions, which can exhibit sharp gradients near the top of the boundary layer [16].

However, current operational RO constellations are typically configured such that opportunities for near-simultaneous sampling capability of moisture in and near convection are limited [17–19]. Examination of the global sampling from the current Formosat-7 Constellation Observing System for Meteorology, Ionosphere, and Climate (COSMIC-2) between September 2019 and May 2021 identified 500 cases where at least two RO were in close spatial (within 200 km of each other) and temporal (10 min separation or less) proximity and receiving the same GNSS satellite telemetry. Using the nearest 30-min Global Precipitation Measurement (GPM) Integrated Merged (IMERG) precipitation products [20], heavy precipitation conditions were defined when the average precipitation rate exceeded

2 mm h^{-1} along the RO ray path. Only 50 cases (about 10%) of RO pairs were identified where one RO intersected the air mass within the heavy precipitation, and its nearby pair intersected an independent air mass path fully outside of the heavy precipitation.

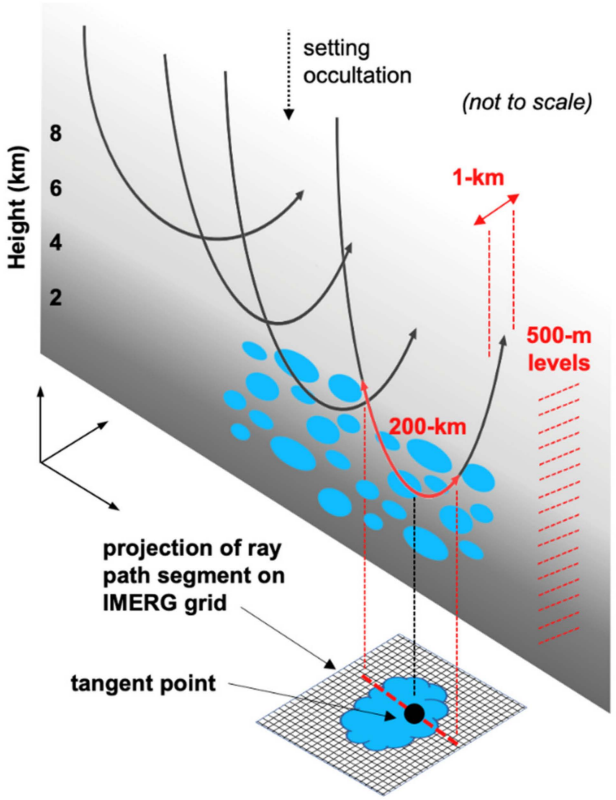


Figure 1. Idealized depiction of a RO setting through a precipitating cloud, showing four ray paths whose lowest level occurs at 8, 6, 4, and 2-km height, and the on-Earth projection of the tangent point of the lowest ray (black symbol). A projection of the 200-km segment of the RO ray path (red dashed lines) nearest the surface is shown on top of the associated surface precipitation estimated by the nearby-time IMERG precipitation data product. The gray shading represents increasing water vapor mixing ratio nearer to the Earth surface. The inherently high resolutions in the vertical and "across-ray" dimension are noted, alongside the coarser path-averaged resolution in the along-ray direction.

Figure 2 depicts one example from 5 May 2020, where the collection of RO-estimated relative humidity (RH) and temperature profiles are contrasted. In this case, three of the COSMIC-2 RO were in near-coincidence near heavy precipitation over the tropical Atlantic Ocean. Each RO captures a different environmental air mass surrounding the convection. The RO ray paths that lie outside of, but within 100 km of the main precipitation are considerably drier than the two RO that fall within the precipitation. While the relative humidity in the boundary layer below 850 hPa (where the majority of the column water vapor is concentrated) is not considerably different amongst all three RO, the relatively smaller amount of water vapor in lower free troposphere (LFT) levels within 850–200 hPa is considerably moistened when compared within the moisture structure nearby. The presence of slight variations in the 100–200 hPa temperature region (dashed lines) is noted (see Section 6 on thermal wind).

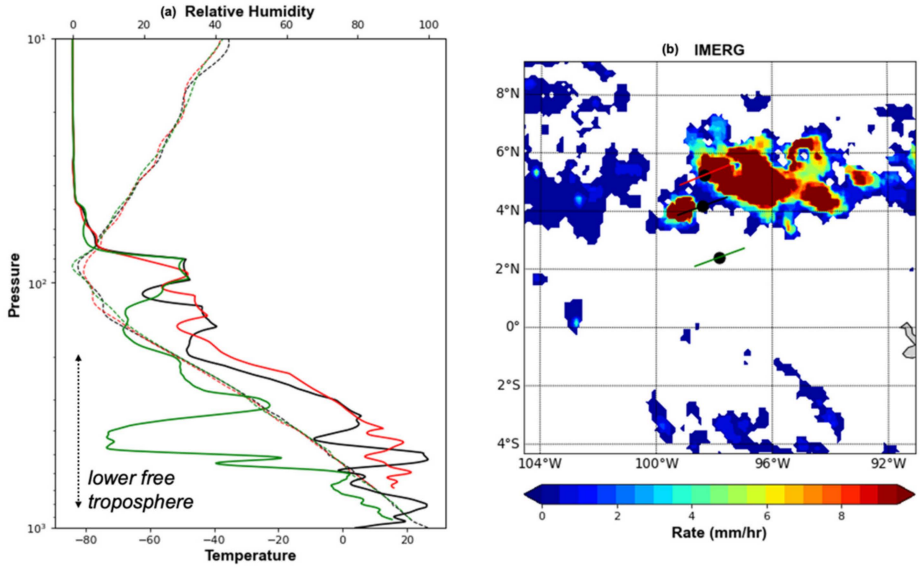


Figure 2. Example of a three-RO coincidence from COSMIC-2 on 5 May 2020. (**a**) Temperature (dashed) and relative humidity (solid lines) profiles from each RO, color-coded according to their location. (**b**). Locations of each of the RO tangent point locations and a 200-km segment of the occultation plane, overlaid on top of the nearest 30-min IMERG precipitation product (the IMERG color scale maximum is set to 10 mm h^{-1} for enhancement). The RO ray path associated outside of the precipitation (green line) is displaced from (and roughly "parallel to") the other two RO ray paths which intersect precipitation (red and black lines).

This present work extends an earlier study by the authors [21], which investigated the basic orbital characteristics of a closely spaced PRO constellation. Section 2 provides the scientific rationale for the PRO constellation observing system. In Section 3, the required number of joint precipitation-moisture profile observations is determined by sampling a large (14 year, 2006–2020) observational dataset from the earlier Formosat-3 COSMIC period. To obtain this number of profile observations, Section 4 investigates different constellation configurations through orbit simulations of PRO opportunities captured from four GNSS telemetries, the Global Positioning System (GPS) operated by the United States Space Force, the Global Navigation Satellite System (GLONASS) operated by Roscosmos, the Galileo system operated by the European Space Agency, and the BeiDou Navigation Satellite System operated by the Chinese National Space Administration (CNSA). Each simulation considers a different number of constellation satellites, satellite temporal spacing (denoted by Δt), orbit inclination and altitude. For each configuration, the required on-orbit time duration is determined, such that the relation between layer-averaged precipitable water vapor and precipitation can be unambiguously discriminated across different tropospheric temperature ranges.

To mitigate uncertainties with the interpretation of the ray-path averaged characteristics of RO, these PRO constellation observations are examined in Section 5 in terms of their spatial and temporal proximity to existing passive microwave (MW) observations taken by operationally sustained low-Earth orbiting satellites, such as the Advanced Technology Microwave Sounder (ATMS) onboard the National Oceanic and Atmospheric Administration (NOAA) Joint Polar Satellite System (JPSS). While the wide-swath (2200 km) ATMS radiometers are exploited for RO assessment [22,23], their observations can also provide additional precipitation context [24] to the constellation PRO observations.

2. Science Rationale

Convective transition statistics serve as model diagnostics for the parameterization of convection in climate and weather forecast models [6,25,26]. These statistics characterize the distribution of precipitation rate (P) as a function of water vapor (denoted by q)

and temperature (T), with the transition to deep convection seen as a threshold in this thermodynamic space where a strong "pickup" of precipitation is noted. Figure 3 shows one example, highlighting the current disparity in the precipitation dependence on water vapor [5] produced by 10 models from the CMIP6 program [27]. Here, conditional averages of precipitation on the LFT water vapor (integrated between two pressure levels, 750 to 900 hPa), and expressed as equivalent water depth in mm), relative to the Atmospheric Radiation Measurement (ARM) best estimate [28] for the Nauru ARM observation site in the tropical Western Pacific, are shown in the following [29]. The layer-integrated water vapor value at which the precipitation pickup occurs has a dependence on temperature that is more complex than constant relative humidity (RH), with larger subsaturation at warmer temperatures [6] (Figure 1), [25]. The relationship between precipitation and water vapor in different free tropospheric layers across the tropical latitudes was investigated by the authors of [7] using globally distributed COSMIC RO temperature and moisture profiles, collocated with GPM IMERG precipitation. Similar to results at specific tropical locations [8,30], sharp pickups of conditionally averaged P as a function of layer q were noted in different tropospheric layers for a variety of tropical ocean and land regions.

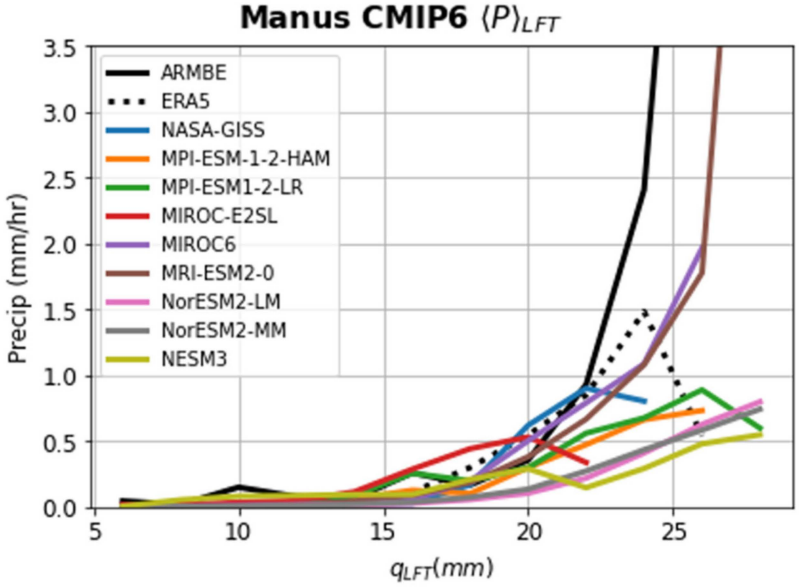


Figure 3. Precipitation rate (mm h^{-1}) conditionally averaged as a function of lower free-tropospheric water vapor q_{LFT} (units of mm) from ten CMIP6 models (colored lines), relative to the ARM Best-Estimate observations (solid black line).

More recent studies have refined this relationship via relative contributions to conditional instability from different free-tropospheric layers above the boundary layer, in terms of dynamic entrainment profiles [8,31,32]. Since these convective transition statistics capture the fast time scale associated with convective development, these diagnostics provide a set of constraints on the convective parameterizations used in climate models [6,29].

For deep convective regions, the precipitation-water vapor-temperature relationships arise from conditional instability of entraining convective updrafts. Figure 4 illustrates the relationship between vertical thermodynamic profiles and conditional stability—this helps to clarify why precipitation dependence on layer-average water vapor and temperature is more complex than simply reaching a saturation value given by the Clausius–Clapeyron relationship. Saturation equivalent potential temperature θ_{es} (which depends only on the temperature profile) is the quantity that a raised convective parcel must exceed to be buoyant. The comparison between this and the profile of equivalent potential temperature θ_e, which is conserved under moist adiabatic motions, provides information on conditional instability for convection. The orange shaded area is closely related to the traditional

Convective Available Potential Energy (CAPE) of a non-entraining cloud parcel raised from the boundary layer. There is growing evidence [4,30,33–35] that models must accurately represent the effects of entrainment of subsaturated air from the lower free troposphere to correctly capture the onset of convection. The impact of this process depends on the subsaturation $(\theta_{es} - \theta_e)$ of the entrained air, indicated in the lower troposphere (900–750 hPa) by the gray area in Figure 4a. The onset of conditional instability in models thus depends on representations of entrainment and correct simulation of the vertical profiles of temperature and moisture and their variations, which in turn interact strongly with the parameterization of convection. Differences between the models and observations can be seen in multiple aspects of the profiles in Figure 4a, reflecting the challenges of this representation in models.

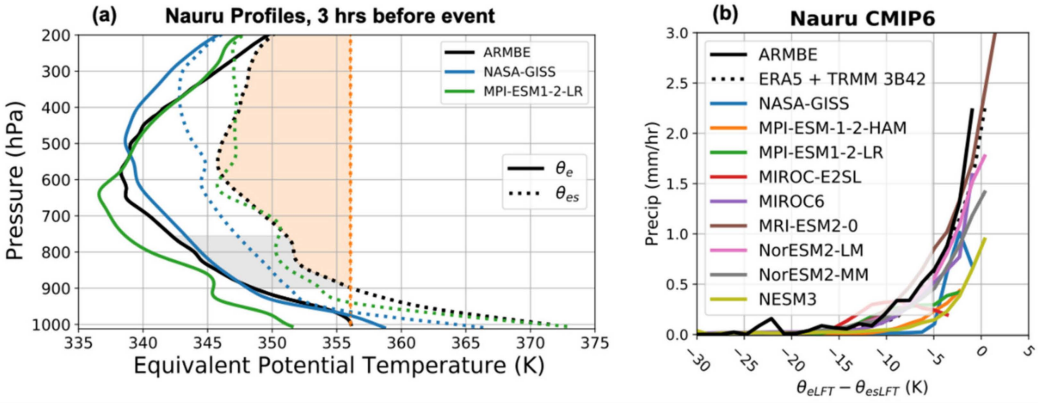


Figure 4. Using vertical profile information to assess convective conditions in CMIP6 models. (**a**) Vertical profiles of equivalent potential temperature θ_e (solid curves) and saturation equivalent potential temperature θ_{es} (dashed curves) at the Nauru island ARM site for the ARM Best-Estimate observations (ARMBE) and two examples of CMIP6 climate models (denoted NASA-GISS and MPI-ESM1-2-LR). The vertical axis is in units of pressure (1 hPa = 100 Pa). The profiles are for conditions 3 h prior to precipitation exceeding 0.5 mm h^{-1}, as a measure of typical profiles associated with onset of deep convection. For the observed curves, the orange shaded area gives a measure of conditional instability for a non-entraining parcel, and the gray area indicates the subsaturation $(\theta_{es} - \theta_e)$ in the lower troposphere (750–900 hPa) that reduces conditional instability when entrained into the convective plume. (**b**) Precipitation conditionally averaged on this subsaturation $(\theta_{es} - \theta_e)$ in the lower troposphere (750–900 hPa layer) for ARMBE observations and several CMIP6 models.

Given the limited structural information contained in satellite datasets, a means to condense this vertical profile information to capture key features of the model deficiencies relative to the convective onset process is desirable. Figure 4b (expanding on analysis in [29] shows an example of a pickup plot for precipitation akin to Figure 3, but conditioned on the subsaturation in equivalent potential temperature that is directly relevant to the impact of entrainment of environmental air into a cloud updraft. While several CMIP6 models simulate the relationship to precipitation reasonably well compared to observations, at least three of the current models have a weak relationship or require environmental conditions too close to saturation to get strong precipitation. A combination of this dependence on subsaturation and dependence on CAPE-like quantities—roughly speaking a weighting of the orange and gray areas in Figure 4a—provides a good empirical predictor of the onset of convection [5,31].

3. Observation Sufficiency to Distinguish the Convective Transition Relationship

Despite demonstrating separation by tropospheric temperature, the number of precipitation-moisture profile observations (hereafter referred to simply as observations) needed to distinguish between convective transition relations has not been quantitatively assessed. This section quantifies the minimum number of observations of joint precipitation and moisture profiles needed to assure that the transition curves for different

temperature ranges can be clearly distinguished. To carry out this analysis requires a large number of joint observations of the precipitation rate P, conditioned on the (T, p, q) profile. For this analysis, existing RO soundings from the abundant Formosat-3 COSMIC period (2006–2020) [36] are combined with the nearest 30-min precipitation estimate from IMERG. This information will then be with considerations from a constellation simulation in Section 4. The global tropical (±20-degree) latitudes are the focus of this investigation, where precipitation is predominantly associated with deep convective systems driven by conditional instability. The relationship between buoyancy and precipitation applies to convective precipitation: If environmental air in the lower free troposphere is sufficiently moist, a convective air parcel is more likely to survive entrainment of environmental air in its ascent [31] yielding strong updrafts and precipitation. The focus on the tropics largely excludes precipitation from extratropical cyclones that obey different dynamics associated with forced uplift in frontal systems—for which evaluation of factors affecting buoyancy from adjacent RO constellation vertical profiles (discussed in Section 5 below) is less relevant. Distinguishing extratropical conditions associated with deep convection is possible in principle, but is more complex and beyond the scope of this paper.

3.1. Separation Using IMERG Precipitation

A bootstrapping procedure [37] was used to resample this COSMIC-IMERG dataset (with replacement) to create many simulated samples with the same size as the original record. This process involves drawing random samples from the original dataset as a means of estimating confidence intervals. Using an average of the water vapor between the 200–850 hPa layer to define the free tropospheric water vapor, conditional average precipitation is determined over thousands of soundings for different temperature ranges. Figure 5 shows one such set of transition curves, representing these data analyzed over the global tropical (±20-degree) latitudes. The black, orange, blue, and red line colors represent the resampled data corresponding to four 1-degree temperature ranges (temperature bins centered at 264, 265, 266, and 267 K, respectively), averaged over the 200–850 hPa layer. Each thin line in each panel represents one realization of conditional-average precipitation rate (mm h^{-1}) as a function of the integrated column water vapor (CWV, units of mm) within the 200–850 hPa layer, showing a nonlinear rise of precipitation with water vapor. This dependence shifts slightly for each temperature (but in a manner more complex than Clausius–Clapeyron, as outlined in Section 2).

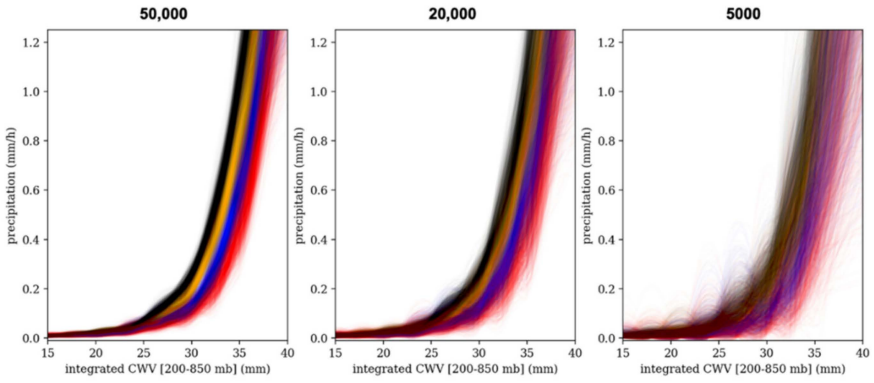


Figure 5. Precipitation rate as a function of 200–850 hPa integrated column water vapor (pickup curves) after (**left**) 50,000 observations, (**center**) 20,000 observations, and (**right**) 5000 observations taken from the COSMIC-IMERG dataset, subsetted into the global ±20-degree latitude range. The black, orange, blue, and red colors refer to observations corresponding to four 1-degree temperature ranges (each centered at 264, 265, 266, and 267 K, respectively), averaged over the same 200–850 hPa layer.

The number on top of each panel in Figure 5 indicates the total number (hereafter denoted by N) of observations used for each temperature range. For N = 5000, there is a hint of separation between these ranges, but one can immediately visualize that discrimination

among neighboring ranges would have low confidence. For N = 50,000 (left panel), the four curves appear to be more clearly separated by the 1-degree ranges. To assess this more quantitatively, an area metric was defined, corresponding to the area between adjacent curves as depicted in Figure 6. A standard statistical method tests the null hypothesis that the area between curves is zero, using the bootstrap ensemble. For this exercise, the area was determined for precipitation rates between 0.3 and 0.5 mm h^{-1} and includes the area between the four temperatures.

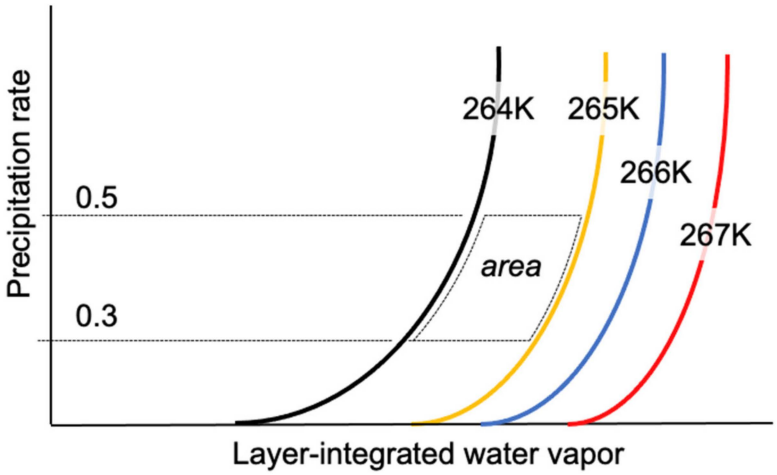


Figure 6. Depiction of the area between adjacent transition curves, used as a metric to separate precipitation-water vapor dependence by different tropospheric temperature ranges. In this depiction the black, orange, blue and red line colors represent a 1-degree different tropospheric temperature range centered at 264, 265, 266 and 267K, respectively. The area between curves for two different temperatures (shown here separating the 264 and 265K range) and between 0.3–0.55 mm h^{-1} is used in the statistical significance tests.

Figure 7 shows the area between the curves as a function of N. The blue line represents the median, and the lower edge of the error-bar is the fifth percentile. The red vertical line at N = 16,000 is where the fifth percentile line crosses the zero-area line, which represents the minimum N needed to separate the four temperature ranges for this entire global tropical area at the 5% confidence level. In other words, when the black curve is above zero, there is over 95% confidence that the curves are distinct.

For particular regions, within the tropical latitudes, the convective transition characteristics are not necessarily the same; different oceanic basins may require a larger (or smaller) value than N = 16,000 noted for the tropical latitudes as a whole. This is because distinguishing the curves depends on the number of samples in high water vapor, strongly precipitating part of the range (the low-precipitation samples are also required but are generally plentiful). Different choices of region can yield less (or more) frequent excursions into such conditions. As one example, Figure 8 shows the same set of transition curves for the West Pacific Ocean domain within ±20-degree latitudes. In this region, the transition curves separate by four 1-degree temperature ranges for a smaller number of observations, between N = 2000 and 10,000.

This procedure was repeated for the East Pacific, Indian, and Atlantic Ocean domains that lie within this same ±20-degree latitude range. For all five regions, the minimum number of observations needed to separate these transition curves for different numbers of temperature ranges was determined. Table 1 tabulates the results, where the number of required observations has been rounded upwards to four values, each indicated with a different color. For example, in the East Pacific Ocean, 5000 observations can distinguish amongst three temperature ranges by 1 K, 10,000 amongst five ranges, and 20,000 amongst six ranges. Since the requirement (discussed below) will be to discriminate the transition curves in each region by at least three temperature bins separated by no more than 1K

(0.5 K in the global tropics), analysis was not done for some of the combinations (gray shaded boxes) once this criterion was reached.

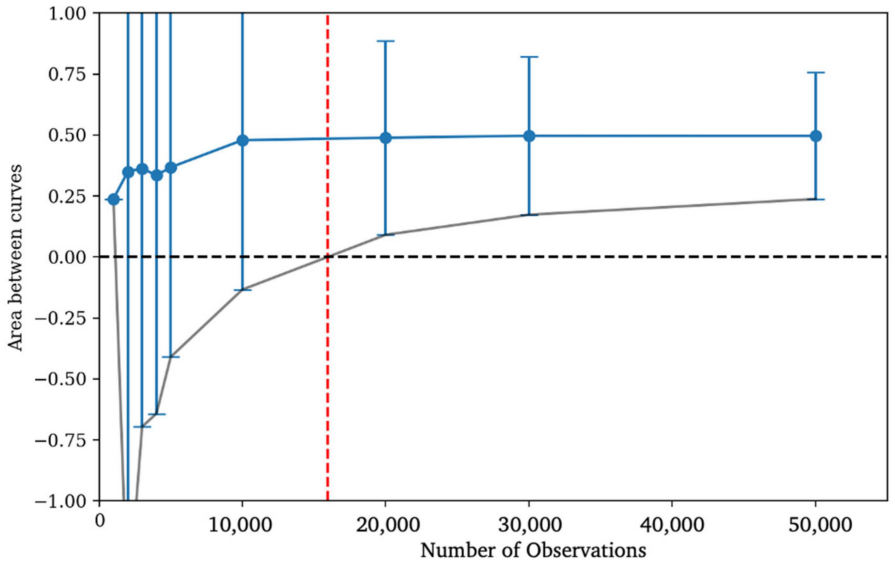


Figure 7. Statistical significance test for the number of soundings required to distinguish between precipitation-water vapor curves to determine data sufficiency. The area metric schematized in Figure 6 is applied to a series of bootstrap ensembles similar to those in Figure 5 to provide a significance test from samplings of the data set as a function of number of observations. The zero crossing of the black curve shows the number of soundings required to achieve the 95% confidence level for distinguishing the curves. Results here are for the whole tropics.

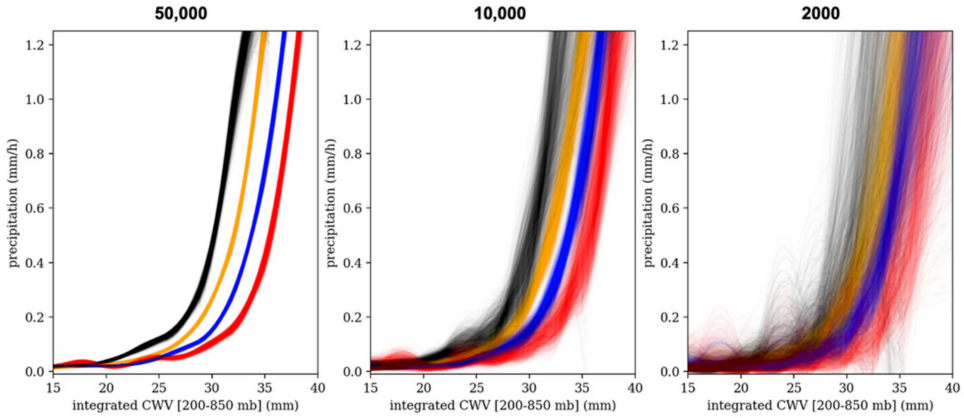


Figure 8. Precipitation rate as a function of 200–850 hPa integrated column water vapor (pickup curves) after (**left**) 50,000 observations, (**center**) 10,000 observations, and (**right**) 2000 observations taken from the COSMIC-IMERG dataset, subsetted into the West Pacific domain. Color scheme otherwise identical to Figure 5.

It is emphasized that even though this temperature separation criterion was defined by the area enclosed within the portion of these transition curves that has substantial conditional-average precipitation, the total number of observations required to separate these curves was drawn from a representative sample that includes all conditions, precipitating or not. This is essential: the increase in the change in precipitation statistics with water vapor reflects a higher probability of precipitation, as well as higher typical intensity [26,29]. Section 4 will examine the required on-orbit time needed by the PRO satellite constellation in order to meet the required observation count for the different oceanic basin regions.

Table 1. Minimum number of joint moisture-precipitation observations (N) needed to separate the transition curves by 0.5 K (global tropics) and 1 K (West Pacific, East Pacific, Indian and Atlantic oceans). The color shading corresponds to N rounded up to the values in the legend (bottom row). The number of rows in the temperature range shading is one less than the number of temperatures listed, since each row represents the number of observations needed to distinguish the temperature indicated from the temperature above. In some regions, insufficient data was available for lowest and highest temperature ranges (e.g., no data below 262 K and above 266 K in the Atlantic Ocean). The gray shading indicates that no analysis was done for this number of temperatures.

Region	Temp (K)	Min Number of Temperatures Discriminated			
		6	5	4	3
Global Tropics (0.5 K)	263 263.5 264 264.5 265 265.5 266 266.5 267				
West Pacific Ocean (1 K)	262 263 264 265 266 267				
East Pacific Ocean (1 K)	261 262 263 264 265 266 267				
Indian Ocean (1 K)	262 263 264 265 266 267 268				
Atlantic Ocean (1 K)	262 263 264 265 266				
N/A		N = 5000	N = 10,000	N = 20,000	N = 30,000

3.2. Separation Precipitation Conditions Using Polarimetric Differential Phase

At the same time that the COSMIC-IMERG dataset was being analyzed, the simulated value of $\Delta\phi$ was computed. This would be the measurable value provided by each PRO constellation satellite to identify the presence of heavy precipitation within the moisture profile. The calculation of the simulated $\Delta\phi$ follows the same procedure described in [21]. At the main GNSS frequency near 1.4 GHz, the specific propagation differential phase shift k_{DP} (units of deg km^{-1}) scales nearly linearly with rain rate R [21] (Equation (1)). Referring

back to Figure 1, k_{DP} was computed for each IMERG grid box intercepted by the lowest 200-km ray path, and $\Delta\phi$ represents its (200-km) path integrated value,

$$\Delta\phi = \sum_{i=1}^{N} k_{DP,i} d_i \quad (1)$$

$$R = \frac{1}{N} \sum_{i=1}^{N} r_i \quad (2)$$

where the subscript i refers to each 0.1-degree IMERG grid box, and N is the number of IMERG grid boxes intercepted by the 200-km path (depicted in Figure 1). While $\Delta\varphi$ cannot provide a unique estimate of the ray path-averaged precipitation (the same $\Delta\varphi$ could occur from different precipitation conditions along the ray path), it can be related to the probability of a precipitation rate being exceeded [14]. Obviously, this is a simplification (short straight-line ray paths, no vertical variation) of the actual ray paths.

The presence of heavy precipitation will be determined from each PRO whenever the measured $\Delta\phi$ exceeds a threshold value. From the representative dataset, Table 2 shows the fraction of the observations that exceed two different $\Delta\phi$ thresholds, for the full global tropics and four sub-basins within these same latitudes. For this study, a threshold of $\Delta\phi > 2$ mm was used as a threshold indicating heavy precipitation. On average, this $\Delta\phi$ threshold corresponds to a path-average rain rate of 2 mm h^{-1} [38].

Table 2. Total number (N) of joint COSMIC-IMERG RO observations in the representative dataset for the global tropical latitudes, as well as four sub-basins contained in the same latitudes. The last two columns indicate the fraction of the total observations where the precipitation conditions were such that the simulated $\Delta\phi$ exceeded a threshold of 1.5 and 2 mm.

Region	Total N RO	($\Delta\phi > 1.5$)/Total	($\Delta\phi > 2$)/Total
Global Tropics	402,549	0.018120	0.013350
West Pacific	59,991	0.027687	0.020320
East Pacific	99,633	0.016802	0.012436
Indian Ocean	61,768	0.018569	0.013583
Atlantic Ocean	55,964	0.009721	0.007469

For example, within the global tropics, in order to separate the transition curves by five temperature ranges as shown in Table 1, 267 of the required 20,000 observations (20,000 × 0.01335) would be required to have $\Delta\phi > 2$ mm. Since this fraction is drawn from a large (>10^7 observations) representative dataset that encompasses a range of precipitating and non-precipitating cases, it can be applied to each satellite orbit constellation tested in Section 4 below to determine the required total number of constellation observations to be collected (and the on-orbit time required).

4. Sampling of Precipitation Conditions for the Constellation Simulation

In this section, various simulated low-Earth orbiting satellite constellation configurations are examined to determine the required orbit time needed to reach the required number of observations determined above. Each constellation is flown over actual IMERG precipitation encompassing the simulation time duration, and the procedure in Section 3.2 is carried out to determine $\Delta\phi$ for each constellation satellite. The $\Delta\phi$ fraction determined from the representative dataset in Section 3.1 is used to estimate the required number of constellation observations needed, and the on-orbit time needed to obtain this number. It is emphasized that the on-orbit time considers idealized data collection and processing yields, whereas actual spacecraft operations and science data quality processing will provide some fraction of this number. This fraction will depend upon the specific spacecraft design and processing algorithms.

The design and sampling characteristics of the PRO constellation simulation have been previously described by the authors of [21], who considered a four-satellite constellation, with the satellites separated by 2 min. Here, constellations of 2, 3, 4, and 8 satellites are considered, at inclinations of 30, 45, and 60 degrees, and orbit altitudes of 475 and 600 km. While a lower inclination orbit concentrates the observations in the desired tropical latitudes, a 98-degree, 800-km sun-synchronous polar orbit was also evaluated, since it is a common orbit for operational weather satellites. A summary of the simulation details is provided in Appendix A.

To show the geographical sampling from this PRO constellation, Figure 9 depicts the projection of the eight PRO ray paths in central Africa for the specific case of the eight-satellite, 60-degree orbit inclination, and 475-km altitude. The sequence of PRO's that result from the satellites receiving the GNSS signal from the same transmitting satellite is denoted as an "event". In this example, the corresponding events cluster together and are assigned a unique color in Figure 9 (the color has no interpretation otherwise). Once the occultation from the first satellite in the constellation initiates, about 2–3 min elapse until the occultation terminates, depending upon the orientation of the occultation ray path relative to the receiving antenna boresight. Several minutes later, the occultation between the second satellite and the same GNSS transmitting satellite starts. This sequence of occultation opportunities then arises for the remaining satellites in the constellation, such that the PRO ray paths are oriented approximately "parallel" to each other (the Earth has rotated underneath the satellites in the intervening time). Such a configuration would capture a time sequence of closely spaced moisture profiles when the constellation flew near and across precipitating weather systems. A "precipitation/environment event" (hereafter denoted by the term P/E event for brevity) is defined as an event that contains at least one PRO that intersects heavy precipitation ($\Delta\phi > 2$ mm) and at least one RO with no precipitation ($\Delta\varphi = 0$), thereby sampling the water vapor profile inside of and in the environment surrounding the heavy precipitation, respectively. The P/E events are the observations that are to be counted towards meeting the requirement from Section 3.

In Table 3, the sampling statistics for the same five regions are presented for a baseline constellation. This baseline constellation is configured with four satellites separated by 2 min, placed into an orbit with an inclination of 45° at a 475-km altitude. To obtain samples representative of the annual cycle, the 10-day simulation was flown in each of December, March, June, and September (40 days total), for a total of 95,212 PRO events. Each satellite assumes a PRO receiver capable of collecting four GNSS telemetries (GPS, GLONASS, Galileo, and BeiDou), for RO events that occur within ±55° antenna azimuth.

Table 3. Number of simulated PRO events for the baseline constellation dataset, for the ±20-degree global tropical latitudes as well as four oceanic basins contained in the same latitude band. The right-most column indicates the fraction of the total events in each region that qualified as P/E events (with at least one occultation inside and outside precipitation), where the precipitation conditions were such that the simulated $\Delta\phi$ exceeded a threshold of 2 mm.

Region	Events in Region	Ratio of Events in Region Relative to Total Constellation Coverage	Fraction Events in Region That Are P/E Events ($\Delta\phi > 2$)
Global Tropics	33,564	0.352	0.0380
West Pacific	5648	0.059	0.0524
East Pacific	9200	0.097	0.0253
Indian Ocean	5056	0.053	0.0411
Atlantic Ocean	5384	0.057	0.0208

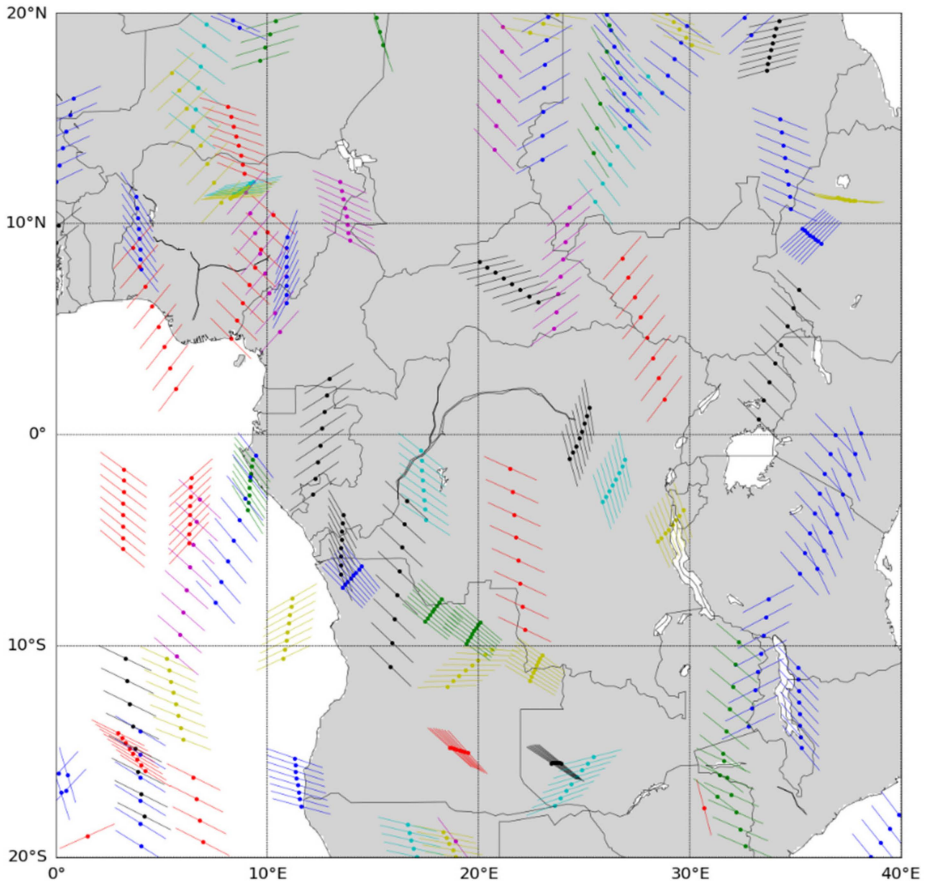


Figure 9. Close-up to the 20 S–20 N, 0–40 E area, showing the TP locations (points) and an associated 200-km ray path segment (lines) for the case when the eight constellation satellites are separated by 2 min, in a 60-degree inclined orbit, 475-km altitude. Each "event" of the 8 satellites is assigned a unique color. These simulated data cover a one-day period and RO opportunities with the GPS, GLONASS, Galileo, and BeiDou GNSS telemetries.

An example is provided to explain the procedure. Table 1 indicates that in the global tropics, 20,000 observations are needed to distinguish five temperature ranges by 0.5 K. From Table 2, this implies that (20,000 × 0.01335) = 267 of these observations are required to exceed the $\Delta\phi$ > 2-mm threshold. In the constellation terminology, each event is one observation. Moving to the constellation in Table 3, the fraction of events that are P/E events is 0.038. Therefore, to meet this requirement, the constellation needs to orbit long enough to collect (267/0.038) = 7024 events in this region. Since the total events listed in Table 3 encompass a 40-day orbit period, this number will be reached after 40 × (7024/33564) = 9 days (rounded up). Since the fraction of the events collected by the constellation in this region is 0.352 (Table 3), after this amount of time the four-satellite constellation will have collected (7024/0.352) = 19925 total observations.

Table 4 tabulates this same procedure for the other regions and different numbers of tropospheric temperature ranges that can be distinguished, using the same $\Delta\phi$ > 2-mm threshold. The number in parentheses indicates the number of on-orbit days (rounded up) needed to meet the N of the required total (i.e., collected by the entire constellation) observations. For clarification, bold font specifies requirements that were obtained from the analysis in Section 3, and normal font specifies the required number using the constellation analysis.

Table 4. For each of the five regions in Table 3, the number of four-satellite baseline constellation observations needed to be collected within the region (N in region) and from the total constellation (N total). Bold font specifies requirements that were obtained from the analysis in Section 3, and normal font specifies the constellation analysis. The associated on-orbit days are indicated in parentheses (rounded upwards) after each value of N total.

Region		Min Required Total Observations			
		30,000	20,000	10,000	5000
Global Tropics (0.5 K)	**N ($\Delta\phi$ > 2)**	**6 temps**	**5 temps**		
	N in region	**400**	**267**		
	N in region	10,526	7024		
	N total	29,900 (13)	19,925 (9)		
West Pacific (1 K)	**N ($\Delta\phi$ > 2)**		**5 temps**		**4 temps**
	N in region		**406**		**101**
	N in region		7748		1928
	N total		131,322 (55)		32,501 (14)
East Pacific (1 K)	**N ($\Delta\phi$ > 2)**		**6 temps**	**5 temps**	**3 temps**
	N (region)		**248**	**124**	**62**
	N (region)		9802	4901	2449
	N (total)		101,055 (42)	50,528 (21)	25,345 (11)
Indian Ocean (1 K)	**N ($\Delta\phi$ > 2)**		**6 temps**	**4 temps**	**3 temps**
	N in region		**271**	**135**	**67**
	N in region		6594	3297	1629
	N total		124,410 (52)	62,205 (26)	30,676 (13)
Atlantic Ocean (1 K)	**N ($\Delta\phi$ > 2)**			**4 temps**	**3 temps**
	N in region			**74**	**37**
	N in region			3682	1779
	N total			64,589 (27)	31,460 (14)

The right-most gray-shaded boxes in Table 4 correspond to the situation whereby the convective transition characteristics can be separated by at least three tropospheric temperature ranges separated by no more than 1 K (0.5 K in the global tropics). In order to meet the value of N total for this criterion, the four-satellite baseline constellation will have to collect measurements for the largest value of the on-orbit days, which is 14 days. Note that the 14-day value is determined by the Atlantic Ocean basin, which is slightly more demanding in terms of the total required observations compared to the other regions.

This procedure was repeated with other variations on the constellation configuration and corresponding values presented in Table 5. For example, a three-satellite constellation would require 28 days to reach the same required total. In general, the required on-orbit time decreases by lowering the constellation inclination angle from 45 degrees to 30 degrees, owing to more on-orbit time concentrated in the desired ±20-degree global tropical latitudes. However, the required time also decreases when increasing the constellation inclination angle from 45 degrees to 60 degrees. This results from the similar orbital inclination to the GNSS satellites (e.g., 55 degrees for GPS), resulting in more RO opportunities than the lower inclination orbits. While an additional orbit altitude of 600 km was simulated (Appendix A), the results are not significantly different from the 475-km altitude.

4.1. Satellite Orbital Separation

An option to increase the number of P/E events for a fixed number of satellites is to increase the orbital separation Δt between the satellites, thereby increasing the spacing between adjacent ray paths. The larger separation between constellation satellites is more likely to locate an "outside" precipitation RO whenever an "inside" precipitation RO is captured, relative to the closer satellite spacing. However, the larger spacing also increases the likelihood that the "outside" heavy precipitation RO is sampling an air mass that is too distant and not representing the environmental air immediate to the heavy precipitation. In this study, a 50–150 km ray path separation is targeted as the desired range. In Appendix A, Table A1 tabulates the fraction of P/E events that occur within this desired ray path spacing.

The data collection time is slightly shorter for the 98-degree, synchronous polar orbit, at the expense of a larger fraction exceeding 100-km ray path separations.

Table 5. Orbital sampling needed to separate three temperatures by 1 K, corresponding to the regions in Table 4. For each constellation configuration, the required number of total events to be collected by the constellation is presented and the corresponding orbit duration (days). S = number of constellation satellites, ϕ is the orbit inclination in degrees, Alt = constellation altitude in km. The satellite temporal spacing Δt between the satellites is fixed at 2 min. The row shaded in gray refers to the baseline simulation used in Table 4.

			Global Tropics		Western Pacific Ocean		Eastern Pacific Ocean		Indian Ocean		Atlantic Ocean	
S	ϕ	**Alt**	**Total Events**	**Days**	**Total Events**	**Days**	**Total Events**	**Days**	**Total Events**	**Days**	**Total Events**	**Days**
8	30	475	5325	3	7705	4	5749	3	8237	4	7847	4
8	45	475	7811	4	11,177	5	9063	4	13,149	6	11,326	5
8	60	475	8660	4	12,508	6	9376	4	15,165	7	11,880	5
8	98	800	6956	3	10,385	5	7183	3	12,285	5	7744	4
4	30	475	14,740	7	23,283	10	17,186	8	23,204	10	24,120	11
4	45	475	19925	9	32,501	14	25,345	11	30,676	13	31,460	14
4	60	475	20,930	9	32,622	14	23,082	10	36,268	15	39,840	16
4	98	800	15,224	6	23,993	10	15,402	6	27,859	11	22,160	9
3	30	475	27,338	12	43,778	19	32,695	14	44,786	19	46,835	20
3	45	475	34,504	15	55,835	24	45,967	20	51,263	22	65,526	28
3	60	475	35,297	15	62,723	25	38,274	16	68,089	28	60,044	24
3	98	800	24,058	10	36,322	14	25,469	10	51,195	20	35,935	14
2	30	475	95,947	41	139,400	59	120,492	51	182,302	77	352,345	149
2	45	475	107,677	45	176,270	74	156,607	66	169,235	71	236,753	74
2	60	475	93,939	38	178,946	71	102,635	41	250,580	100	143,702	57
2	98	800	58,948	23	97,450	38	58,120	23	131,733	51	96,391	38

4.2. Constellation Design Considerations

As mentioned earlier, the results in Table 5 assume an idealized collection of all occultations arising from all transmitting satellites of the four GNSS satellite systems. Overall net yield fraction was not considered, since these characteristics are unique to a specific spacecraft and PRO receiver design, and data processing algorithms. Here, a set of reasonable assumptions are made to provide a realistic duration of the constellation data collection period.

A conservative estimate for net yield from both satellite operations and data processing of 50% is assumed, where each RO needs to provide data to at least the 850 hPa level. This consideration would extend the required four-satellite baseline constellation collection period to (14/0.5) = 28 days (assume one month).

At any given time, each PRO receiver is tracking multiple occultations from the GNSS satellites that are within its antenna field of view. If all four telemetries are tracked, this number can be as high as 10 at any one time (Figure A4 in Appendix A), and each PRO requires two (H and V) receive channels. Assuming the PRO receiver on each of the constellation satellites can track up to four PROs at any one time, only 70% of the total would be collected. Another option is to track only two GNSS telemetries (GPS + GLONASS) instead of all four, which would capture nearly all (95%) of the available occultations. These receiver characteristics would double the overall collection period to 2 months.

Lastly, it is important to add an overall margin on top of this analysis, to account for unexpected conditions leading to missing data. Assuming a conservative 50% margin, this leads to an overall collection period of 3 months. If a three-satellite constellation at the same

475-km altitude was used, this number would roughly double (Table 5), to approximately 6 months.

Another consideration is the operation period. The simulations sampled IMERG precipitation spread across different months of the year in order to represent seasonality, but actual operations may occur in specific months of the year where precipitation is more or less frequent. The inclined orbits will capture the variability in the diurnal cycle (not examined in this study). Using the GPM satellite as an example (65-degree inclination), a 60-degree constellation inclination would sample a full diurnal cycle approximately every two months. This provides an additional consideration, independent from the sufficiency calculations above.

5. Joint Observations with Operational Passive MW Radiometers

In the above analysis, a $\Delta\varphi > 2$ threshold was used as an indication of heavy precipitation, but the ray-path nature of the RO observation provides little detail on horizontal context. For example, a RO ray path could exceed the $\Delta\phi$ threshold but in reality may have traversed through an edge of a convective cloud system, not necessarily indicative of the moisture structure within the convective core region associated with strong vertical air motion. Strong convection lofts heavy precipitation above the freezing level. In ROHP data, large $\Delta\varphi$ are commonly noted well above 10-km altitude in convective clouds [39]. Heavy precipitation is often associated with horizontal moisture gradients. For example, if the successive RO ray paths were oriented parallel to and spread across a frontal boundary (some RO capture the dry side; other RO the moist side), the surrounding moisture structure will be interpreted differently than if the RO were aligned in a more perpendicular orientation relative to the front (similar moisture captured across all RO).

To gather two-dimensional context on the clouds at the time of the constellation overpass, one option is to consult fast-refresh geostationary satellite imagery. The current network of geostationary satellites has common channels in the longwave (near 11 μm) for tracking the day/night evolution of optically thick cloud tops [40]. With their wide (>2000 km) swath, existing operational passive MW radiometric observations can complement the constellation observations, providing horizontal precipitation context, and an estimate of the condensed water path along the RO ray paths [24].

Figure 10a provides one coincidence intersection from a simulated PRO event and a passive MW overpass occurring on 6 August 2018 near 1320 UTC, showing eight occultations, depicting 200-km ray path segments centered at each of the eight TP locations, and the corresponding (descending node) ground track of each simulated PRO satellite. These are overlaid upon the 165.5 GHz brightness temperature (TB) imagery from the Advanced Technology Microwave Sounder (ATMS) during a descending pass of the Joint Polar Satellite System (JPSS) NOAA-20 satellite near 1405 UTC. In this example, the simulated PRO events are just to the left of the satellite orbit track direction (i.e., negative antenna azimuth angle). Using TB < 200 K as a proxy for heavy precipitation, the PRO from satellite 1 traverses the region of heavy precipitation, those from satellites 2 and 3 traverse the edge of the precipitation, and those from satellites 4–8 form the outside-precipitation (surrounding environment) observations (an example of a P/E event). The TB imagery provides horizontal context to the precipitation structure and can be used to depict the water vapor structure in the cloud-free areas away from the precipitation. In this example event, each RO ray path segment was oriented such that was <500 km from the ground track of its respective satellite. However, other events will exhibit a range of offsets, depending upon the relative locations of the satellites during the occultation time. Figure 10b shows the distribution of the maximum value of the distance from the receiving satellite subtrack and the endpoints of each ray path segment (Figure A1 in Appendix A). The solid red line represents the cumulative fraction, showing that 90% of the events fall within 2000 km of the satellite subtrack. Since the event could lie to the left or right side relative to the spacecraft velocity vector, this implies that a single passive MW radiometer with a swath width of 4000 km would be needed to cover this same percentage, a value which is

technically unfeasible from typical low-Earth orbit satellite altitudes < 800 km. However, a swath width of 1500 km would cover approximately 30% of the events.

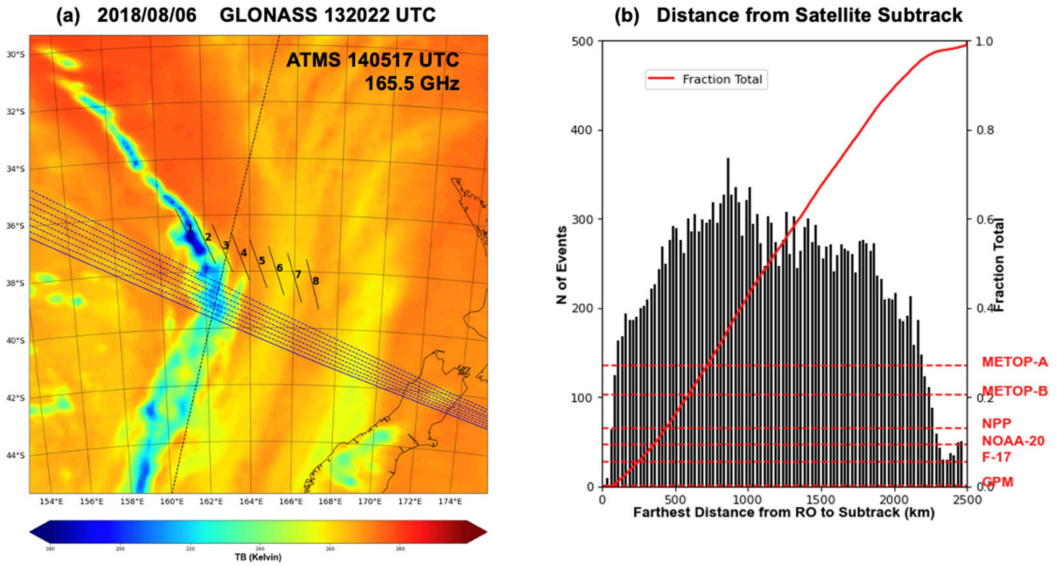


Figure 10. (**a**) A P/E event from GLONASS occurring near 132022 UTC on 6 August 2018, from a simulated eight-satellite constellation. The location is the Tasman Sea between Australia and New Zealand. The associated PRO locations are numbered alongside the associated 200-km ray path, overlaid upon the ATMS 165 GHz TB from the NOAA-20 overpass at 140517 UTC. The orbit track of NOAA-20 is in the dashed black line. The descending orbit tracks of each of the receiving satellites are shown in the blue dashed lines (the leading satellite 1 is a solid line). (**b**) The distribution of events as a function of the maximum value of the distance from the receiving satellite subtrack and the endpoints of each ray path segment (left vertical axis). The solid red line represents the cumulative fraction (right vertical axis). The series of horizontal dashed lines indicate the equivalent cumulative fraction coverage that can be provided by passive MW sensors onboard current satellites (lowest line = GMI only, next line above = GMI + DMSP F-17 SSMIS . . . , highest line = all six sensors. The satellite and sensor names are as follows: DMSP = Defense Meteorological Satellite Program, NPP = National Polar Orbiting Partnership, JPSS = Joint Polar Satellite System, GPM = Global Precipitation Measurement. The Special Sensor Microwave Imager Sounder (SSMIS) is the passive MW sensor on the DMSP F-17 satellite, the Microwave Humidity Sounder (MHS) onboard the MetOp satellites, the GPM Microwave Imager (GMI) onboard the GPM satellite, and the Advanced Technology Microwave Sounder (ATMS) onboard the NPP and NOAA-20 satellites.

To quantify what percentage could be captured using data from five current operational satellites plus one research satellite (i.e., GPM), the near-coincident passive MW coverage was assessed during the entire 40-day simulation period. This was done by checking for passive MW swath coverage from each of the passive MW satellites in succession (Figure 10 caption) until coverage (of all eight 200-km ray paths) was located within ±15 min. The horizontal dashed lines in Figure 10b show the accumulated coverage when the passive MW satellites are considered in succession. For example, there are very few intersections between the RO ray paths and GPM, and with this satellite alone the total coverage is <1%. If GPM and the SSMIS onboard the DMSP F-17 satellite are considered, the total coverage rises to 5%. When all six satellites are considered, the fractional coverage is about 26%, which is nearly commensurate with the 1500-km radiometer swath.

6. Discussion

A small constellation of PRO observations is proposed as a means to obtain independent, observational verification of the convective transition behavior exhibited amongst

multiple climate models and to assess this transition across multiple tropical regions. A resampling method was carried out to ascertain the required minimum number of observations using real-world observations from COSMIC RO and the GPM IMERG precipitation. The number of profile observations (N) required to discriminate the convective transition relationship by 1K tropospheric temperature was determined for each of five tropical oceanic regions. The results show that N is between 5000 to 30,000 observations, depending upon the oceanic region, with more observations required for the tropical Atlantic Ocean.

Orbit simulations were carried out to determine how many joint precipitation and environment (P/E) events would result from a constellation of satellites, each separated by 2 min, defined where at least one PRO observation captures a heavy precipitation event and at least one other PRO observation captures the region outside of the heavy precipitation. The 30, 60, and 98-degree orbit inclinations provide slightly more data during this same period relative to the 45-degree inclination. An inclination of 30 degrees concentrates the observations in the preferred $\pm$20-degree tropical latitudes, and the 60-degree inclination is closer to the inclination of the GNSS satellites. While the 98-degree inclination provides the largest fraction of events exceeding 100-km separation distance, it would lack the capability to sample across the diurnal cycle. A 475-km altitude, 45-degree inclination baseline orbit represents a tradeoff between a slightly longer orbit duration with the advantage of a higher percentage of P/E events possessing the desired 50–150 km ray path separation distance. There is very little difference in these values if the orbit altitude is raised from 475 km to 600 km.

With the ability of the RO observation to profile the temperature along each ray path, the separation of the first and last satellites provides an additional opportunity to estimate (one component of) the profile of the thermal wind (up to a constant of integration), in the geostrophic approximation. The thermal wind is the wind that flows parallel to the temperature gradient in the troposphere, away from the boundary layer where drag effects are significant. The thermal wind speed will be a function of how strong the temperature gradient is, and will be a good approximation of the wind in the subtropical latitudes poleward. Such a technique has been used from Mars Global Surveyor (MGS) radio occultation data, where RO profiles from successive orbits were used to infer winds using geostrophic balance [41].

The polarimetric RO constellation data are proposed and examined here for scientific purposes related to climate and forecast model evaluation. It is noted that at this time (late 2021) COSMIC-2 data are yet fairly recent, but have already been used for assessing model differences in the densely sampled tropical latitudes [42]. Since the sequence of PRO would provide a measure of precipitation location in the vertical and (the across-ray component of) horizontal directions, there may also be advantages in flying PRO receivers in a closely spaced formation for NWP data assimilation purposes, but this impact has not been assessed. While RO forward operators that simulate the bending angle profile are used at major operational weather centers [43], currently no forward operator has been developed to model the associated polarimetric phase profile from the model analysis state.

7. Conclusions

Assuming that occultations from two GNSS telemetries are tracked, a 50% data processing yield with added 50% margin, the convective transition relationships can be distinguished by three tropospheric temperatures separated by 1 K, with a six-month on-orbit duration from a constellation of at least three satellites. The satellites orbit in a single plane at a 475-km altitude, 45-degree inclination orbit with a 2-min spacecraft separation. In actual satellite operations, the actual data collection and orbit duration will depend upon unique design factors such as power limitations, orbit maintenance, and PRO receiver characteristics.

Near-coincident passive MW coverage from the current operational passive MW satellite constellation was examined as a means to add horizontal context to the interpretation of the ray-path observations from each PRO. Further examination of the coincident events showed that ~26% are associated with near time-coincident passive MW coverage from six

passive MW imagers or sounders onboard current operationally sustained platforms. The utility of the passive MW data was assessed solely by swath coverage and did not extend to the choice of the associated MW channels or sampling of the precipitation diurnal cycle, which are beyond the scope of this study. If a PRO constellation was flown in loose formation with an operationally sustained wide-swath (>2000 km) passive radiometer (such as the JPSS polar-orbiting platforms), it would yield a large fraction of near-coincident RO and passive MW observations. Such a distributed observing strategy would capitalize upon the advantages of small satellite observations (unique observational capability, limited sampling, short expected lifecycle) with the reliability of sustained, reliable operational platforms (established observations, dense sampling, long lifetime), to utilize near-coincident observations as the respective satellite orbit paths intersect in close time proximity [44].

Author Contributions: Conceptualization, F.J.T., R.P. and J.D.N.; methodology, F.J.T., R.P. and J.D.N.; software, F.J.T., R.P. and D.D.M.; validation, R.P., F.J.T. and D.D.M.; formal analysis, F.J.T., R.P., J.D.N. and T.E.; investigation, F.J.T., R.P. and J.D.N.; resources, F.J.T., R.P. and J.D.N.; data curation, F.J.T., R.P., J.D.N. and T.E.; writing—original draft preparation, F.J.T. and J.D.N.; writing—review and editing, F.J.T., R.P. and J.D.N.; visualization, F.J.T., R.P., J.D.N. and T.E.; supervision, F.J.T. and J.D.N.; project administration, F.J.T., R.P. and J.D.N.; funding acquisition, F.J.T., R.P. and J.D.N. All authors have read and agreed to the published version of the manuscript.

Funding: The work conducted at ICE-CSIC/IEEC was supported by the Spanish grant ESP2015-70014-C2-2-R. The research by RP was funded by the Spanish Ministry of Science, Innovation and Universities grant number RTI2018-099008-B-C22/AEI/10.13039/501100011033/FEDER, EU. RP has received funding from the postdoctoral fellowships programme Beatriu de Pinós, funded by the Secretary of Universities and Research (Government of Catalonia) and by the Horizon 2020 programme of research and innovation of the European Union under the Marie Sklodowska-Curie grant agreement No 801370. F.J.T. acknowledges support from NASA US Participating Investigator (USPI) program element 14-ESUSPI14-0014. J.D.N. and T.E. are supported in part by the National Science Foundation grant AGS-1936810.

Data Availability Statement: IMERG precipitation data and GPM partner passive MW data are publicly available from NASA's Precipitation Processing System Science Team Online Request Module (STORM) at https://storm.pps.eosdis.nasa.gov/storm (accessed on 28 January 2022). COSMIC and COSMIC-2 data are publicly available from the COSMIC Data Analysis and Archive Center (CDAAC) at https://cdaac-www.cosmic.ucar.edu (accessed on 28 January 2022).

Acknowledgments: This work was carried out at the Jet Propulsion Laboratory, California Institute of Technology, under a contract with the National Aeronautics and Space Administration. © 2022. All rights reserved.

Conflicts of Interest: The authors declare no conflict of interest. The funders had no role in the design of the study; in the collection, analyses, or interpretation of data; in the writing of the manuscript, or in the decision to publish the results.

Appendix A

The design and configuration for the polarimetric RO constellation simulations is described in Turk et al. (2019). In this appendix, a brief summary is provided for reference.

A constellation of eight satellites, separated by 2 min, run for a 10-day simulation, sampling 10-day precipitation at 3-month intervals throughout one year (2018) to capture seasonal variability. Each simulation captures the fore (rising) and aft (setting) RO opportunities that occur between each constellation satellite and the GNSS transmitting satellites (telemetries transmitted by each of the GPS, GLONASS, Galileo, and BeiDou satellites). The propagation path (i.e., the line between the transmitting and receiving satellite) are sampled once per second from which the trace of the on-Earth tangent points (TP) and the resulting ray path coordinates and orientation (i.e., the azimuth angle of the ray path relative to the antenna boresight) are derived. From this eight-satellite simulation, selected satellites can be "omitted" in order to evaluate how PRO sampling of precipitation conditions varies with a smaller number of constellation satellites or a longer time separation. The procedure

described in Section 3.2 is used to calculate the $\Delta\phi$ that would occur from the sampling of precipitation conditions provided by the nearest 30-min IMERG precipitation dataset.

Figure A1 shows a pictorial of one "event", an event being defined as all when all satellites are considered to collect a PRO from the same transmitting GNSS satellite. This example is an event from eight satellites. The closest-to-Earth TP locations are shown from each of the eight receiving satellites (each with a different color), and the corresponding receiving satellite ground track (same color as the TP). A "precipitation + environment" event (P/E event) occurs when one or more satellites detects heavy precipitation ($\Delta\phi > 2$) and another detects no-precipitation ($\Delta\phi = 0$). The TP locations are separated by a distance d. However, the actual propagation ray paths associated with each RO in general lie in a different direction depending upon the position of the transmitting and receiving satellites during the RO duration, given by the angle α. Therefore, the "effective" separation between the ray paths (d_{eff}) is smaller, given by $d_{eff} = d\cos(90^o - \alpha)$.

The ray path lines represent the path upon which the corresponding air mass thermodynamics would be sampled from each constellation satellite. For convective science purposes, what is important is the value of d_{eff} since it determines the ray spacing. For example, if the angle α approaches zero, the ray paths become packed closer together. If one of the RO captured a heavy rain event, the remaining RO ray paths are too close by and will not adequately sample the horizontal water vapor gradient, capturing the environmental air mass external to the heavy precipitation. While there is no specific value of d_{eff} that captures the moisture variability surrounding convective precipitation, a desired 50–150 km range of d_{eff} is considered for this investigation.

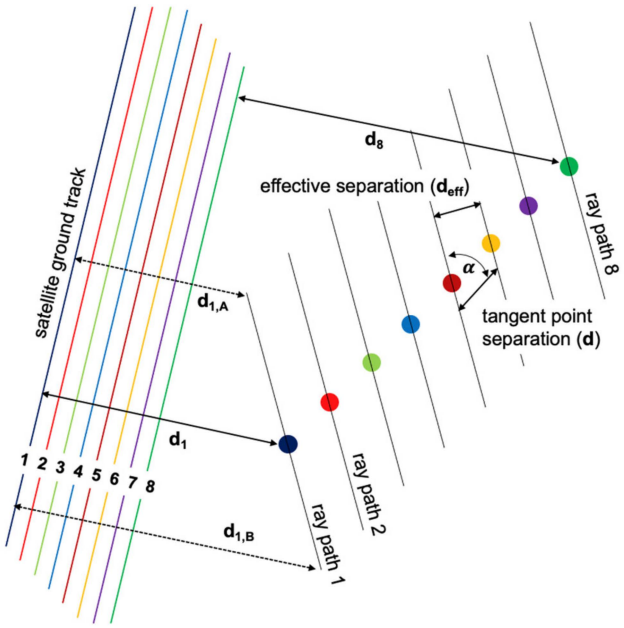


Figure A1. Geometry of one eight-satellite RO event. The tangent points (TP) are shown from each receiving satellite (each with a different color), and the corresponding satellite (1, 2, . . . , 8) ground track is in the same color. The distance d_1 corresponds to the closest distance between the first RO and the subtrack of its corresponding receiving satellite. In this example, d_{1A} and d_{1B} represent the distance from the subtrack of satellite 1 to each endpoint of a 200-km ray path segment, and d_{1B} is the larger of these. This process is repeated for all satellites, and the largest overall value is plotted in the histogram shown in Figure 10b.

As one example, Figure A2 summarizes the global statistics for an eight-satellite constellation at a 475-km altitude, 30-degree inclination orbital plane, 2-min satellite spacing and a PRO receiving capable of collecting rising and setting occultations from four GNSS, telemetries, over the 40-day period. Assuming a maximum antenna azimuth angle of 55

degrees, a total of 93,108 events were collected. Figure A2a,b present the histogram of the separation distance (d) and angle α, respectively. The separation distance peaks near 70 km, and the relative angle peaks near 5 degrees and slowly drops off. When the resulting effective separation (d_{eff}) is considered (Figure A2c), the peak near 70-km shifts to separate clumps near 10, 40, and 70 km (i.e., ray paths are closer to each other). When considering only P/E events (Figure A2d), about 44% of these fall within the 50–150-km range with a rather uneven distribution, weighted towards separations < 100 km.

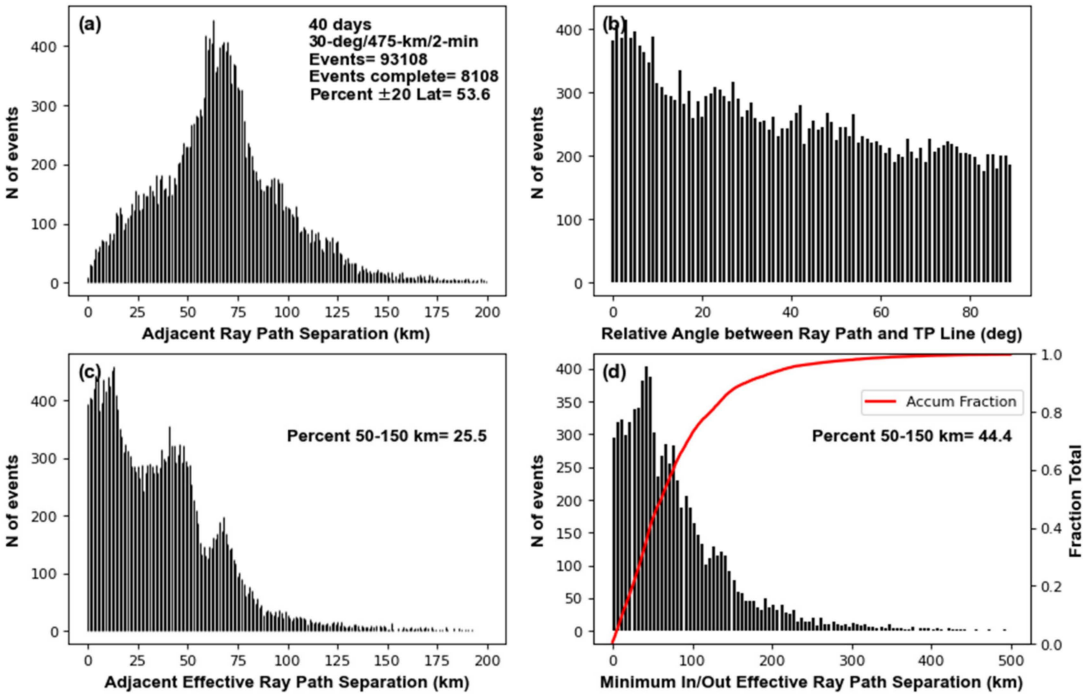


Figure A2. Summary statistics for the eight-satellite constellation in the 30-degree, 475-km orbit. (**a**) Histogram of the separation distance (d). (**b**) Histogram of the relative angle between the ray path and TP line (α in Figure A1). (**c**) Histogram of the effective separation (d_{eff}). (**d**) Histogram of the minimum d_{eff} for the P/E events.

Figure A3 shows an identical format as Figure A2, but for the 98-degree, 800-km sun-synchronous polar orbit. Slightly more events (102,284) were captured. However, this advantage comes at the cost of more orbital time spent at higher latitudes, where heavy precipitation is less frequent. The angle α is clumped more near 80 degrees (Figure A3b), leading to a broader distribution in adjacent effective ray path separation (Figure A3c) roughly centered near 80 km. In general, the 98-degree orbit exhibits a larger separation between successive RO ray paths, owing to its more north-to-south descending orbit path. About 50% of the P/E events fall within the 50–150-km separation range (Figure A3d) with values weighted past 100 km (opposite of Figure A2).

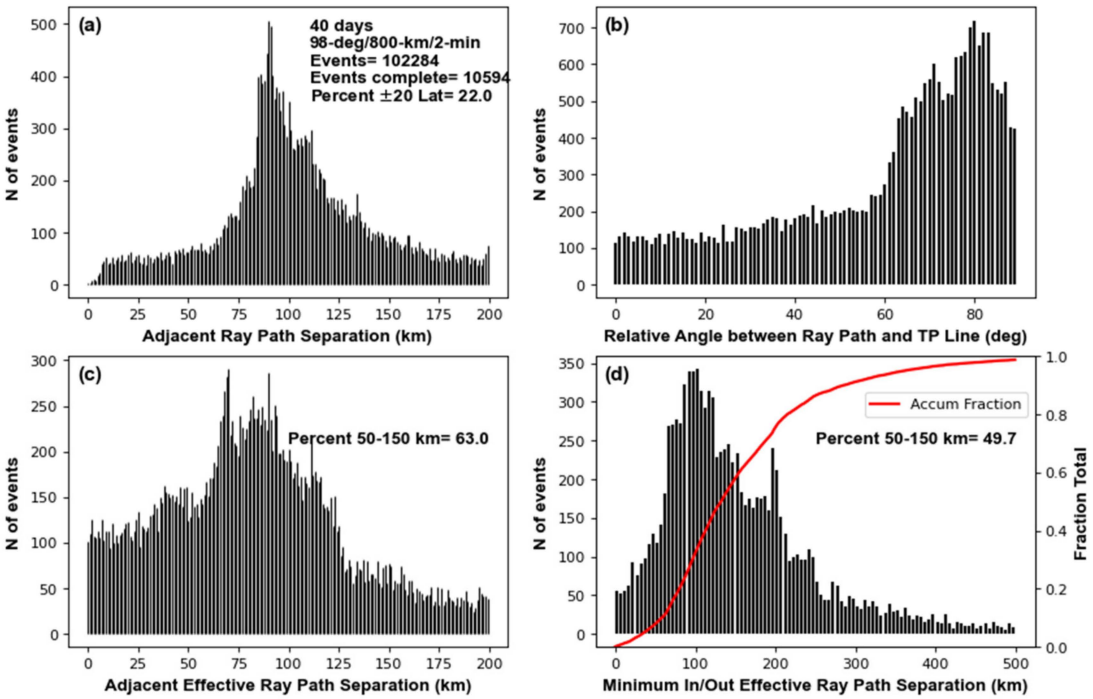


Figure A3. Same as Figure A2, but for the 98-degree, 800-km sun-synchronous polar orbit. (**a**) Histogram of the separation distance (d). (**b**) Histogram of the relative angle between the ray path and TP line (α in Figure A1). (**c**) Histogram of the effective separation (d_{eff}). (**d**) Histogram of the minimum d_{eff} for the P/E events.

Table A1 summarizes the global simulation results for different numbers of satellites in the constellation (C1) and orbit inclination and altitude (columns C2 and C3). The number of events (C4) does not change significantly, and as one would expect the fraction of these that are P/E events drops off with a smaller number of satellites. The key metric is column C9, the number of P/E events collected per day (C9 = C4 × C6 × C7). Column C8 presents the fraction of P/E events that fall within the desired 50–150 km ray path spacing between the "inside" and "outside" precipitation PRO. These findings can be summarized as follows:

1. The fraction of events that are P/E events quickly drops off as the number of satellites in the constellation is reduced.
2. The effective separation between each of the ray paths tends to decrease as the orbit inclination decreases. For a 30-degree inclination, a spacecraft separation Δt of 4-min increases the number of events with a larger value of d_{eff} and nearly doubles the number of P/E events, compared to the Δt = 2-min separation.
3. A constellation placed into a 60-degree inclination collects slightly more events than one at 30- or 45-degree inclination. This occurs since the GNSS transmitting satellites orbit in a ~55-degree inclination, and the transmitting and receiving satellites are in view slightly more often.
4. A polar orbit collects slightly more events than any of the inclined orbits, but also the largest fraction of events whose effective separation exceeds 100 km. Unlike the inclined orbit, these observations would not sample the precipitation diurnal cycle.

Table A1. Summary of global sampling of events, and the fraction that is P/E events, by different numbers and spacing of satellites in various constellation configurations over the simulated 40-day period. Rising and setting occultations with GPS, GLONASS, Galileo, and BeiDou GNSS satellites are considered. S = number of satellites in the constellation, ϕ = orbit inclination in degrees, Alt = constellation altitude in km, and the satellite temporal spacing (minutes) is denoted by Δt. The gray-shaded row (S = 4, Δt = 2) is the baseline constellation considered in this manuscript.

C1	C2	C3	C4	C5	C6	C7	C8	C9
S	**ϕ**	**Alt**	**Total Events**	**Frac Total Events >100-km Spacing**	**Frac Total Events ($\Delta\phi$ > 2)**	**Frac Total Events ($\Delta\phi$ > 2) P/E Events**	**Frac P/E Events 50–150 km Spacing**	**P/E Events Per Day**
S = 8 Δt = 2	30	475	93,108	0.035	0.106	0.820	0.443	203
	30	600	91,304	0.043	0.115	0.850	0.458	223
	45	475	93,548	0.034	0.108	0.869	0.532	219
	45	600	91,040	0.047	0.108	0.874	0.528	216
	60	475	98,408	0.107	0.109	0.894	0.523	239
	60	600	96,324	0.135	0.108	0.895	0.509	234
	98	800	102,284	0.350	0.112	0.925	0.496	265
S = 4 Δt = 2	30	475	94,512	0.038	0.068	0.490	0.464	80
	30	600	92,228	0.046	0.072	0.520	0.475	87
	45	475	95,212	0.036	0.067	0.559	0.583	91
	45	600	92,488	0.049	0.067	0.571	0.576	90
	60	475	100,100	0.108	0.066	0.614	0.540	101
	60	600	98,152	0.139	0.066	0.620	0.529	101
	98	800	103,536	0.351	0.067	0.702	0.497	123
S = 4 Δt = 4	30	475	93,424	0.275	0.086	0.726	0.468	146
	30	600	91492	0.332	0.092	0.760	0.449	161
	45	475	93,924	0.422	0.085	0.789	0.483	159
	45	600	91,376	0.444	0.085	0.791	0.463	153
	60	475	98,856	0.547	0.082	0.823	0.371	169
	60	600	96,884	0.547	0.083	0.818	0.344	165
	98	800	102,644	0.757	0.081	0.861	0.210	180
S = 3 Δt = 2	30	475	94,916	0.038	0.058	0.319	0.462	44
	30	600	92,500	0.045	0.061	0.351	0.471	50
	45	475	95,628	0.037	0.056	0.386	0.620	53
	45	600	93,060	0.050	0.056	0.392	0.627	52
	60	475	100,604	0.110	0.054	0.442	0.571	60
	60	600	98,592	0.139	0.055	0.446	0.552	61
	98	800	103,892	0.350	0.054	0.533	0.531	76
S = 2 Δt = 2	30	475	95,228	0.039	0.047	0.121	0.448	14
	30	600	92,724	0.046	0.050	0.148	0.472	17
	45	475	95,980	0.037	0.045	0.160	0.636	18
	45	600	93,584	0.051	0.045	0.165	0.634	18
	60	475	100,976	0.111	0.042	0.206	0.626	22
	60	600	98,968	0.141	0.043	0.208	0.637	23
	98	800	104,204	0.351	0.042	0.273	0.634	30

In Table A1, an idealized data collection was assumed, implying that all available occultation opportunities were captured. In actual operating conditions, this is not the case (further discussed in Section 4.2). At any given time, each PRO receiver will have multiple GNSS occultation opportunities within the broad antenna field of view. Figure A4 shows the cumulative normalized histogram of the number of occultations that occur for different PRO receive capabilities.

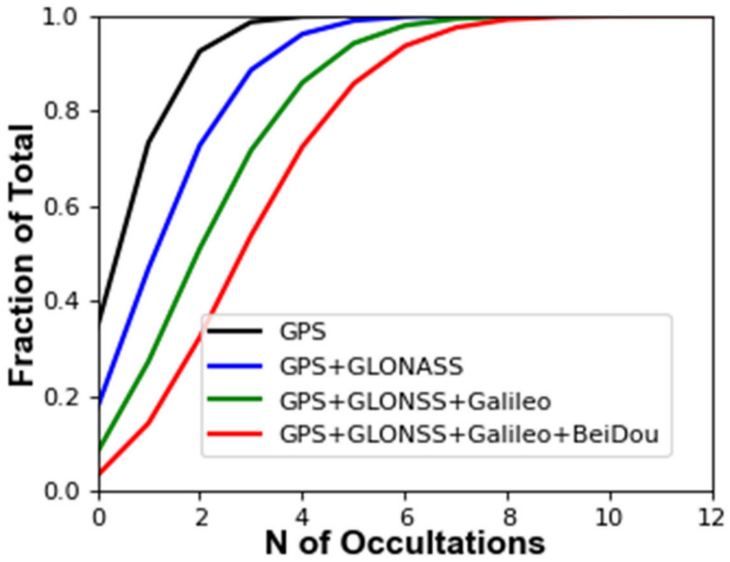


Figure A4. Cumulative distribution of the number of occultation opportunities that are available at any given time, to a PRO receiver capable of capturing only GPS telemetry (black), GPS + GLONASS (blue), GPS + GLONASS + Galileo (green), and GPS + GLONASS + Galileo + BeiDou (red).

A PRO receiver capable of only GPS capture is shown in the black line, whereas a PRO receiver capable of all four telemetries is shown in the red line. Note that in this latter case, there can be up to 10 occultations (rising or setting) that are available to be captured, and for a PRO measurement there are two channels (H and V) required. With only two telemetries (GPS and GLONASS), no more than four occultation opportunities occur nearly all of the time. If onboard processing software, antenna, or hardware limitations are a consideration, this factor will need to be taken into consideration.

References

1. Rio, C.; Del Genio, A.D.; Hourdin, F. Ongoing Breakthroughs in Convective Parameterization. *Curr. Clim. Chang. Rep.* **2019**, *5*, 95–111. [CrossRef]
2. Schiro, K.A.; Neelin, J.D.; Adams, D.K.; Lintner, B.R. Deep Convection and Column Water Vapor over Tropical Land versus Tropical Ocean: A Comparison between the Amazon and the Tropical Western Pacific. *J. Atmos. Sci.* **2016**, *73*, 4043–4063. [CrossRef]
3. Sahany, S.; Neelin, J.D.; Hales, K.; Neale, R.B. Temperature–Moisture Dependence of the Deep Convective Transition as a Constraint on Entrainment in Climate Models. *J. Atmos. Sci.* **2012**, *69*, 1340–1358. [CrossRef]
4. Kuo, Y.-H.; Neelin, J.D.; Mechoso, C.R. Tropical Convective Transition Statistics and Causality in the Water Vapor–Precipitation Relation. *J. Atmos. Sci.* **2017**, *74*, 915–931. [CrossRef]
5. Ahmed, F.; Neelin, J.D. A Process-Oriented Diagnostic to Assess Precipitation-Thermodynamic Relations and Application to CMIP6 Models. *Geophys. Res. Lett.* **2021**, *48*, e2021GL094108. [CrossRef]
6. Kuo, Y.-H.; Neelin, J.D.; Chen, C.-C.; Chen, W.-T.; Donner, L.J.; Gettelman, A.; Jiang, X.; Kuo, K.-T.; Maloney, E.; Mechoso, C.R.; et al. Convective Transition Statistics over Tropical Oceans for Climate Model Diagnostics: GCM Evaluation. *J. Atmos. Sci.* **2020**, *77*, 379–403. [CrossRef]
7. Padullés, R.; Turk, F.J.; Ao, C.O.; de la Torre-Juárez, M.; Kuo, Y.-H.; Neelin, J.D. Global tropics precipitation relationships to free tropospheric water vapor using radio occultations. *J. Atmos Sci.* 2021; *in review*.
8. Schiro, K.A.; Neelin, J.D. Deep Convective Organization, Moisture Vertical Structure, and Convective Transition Using Deep-Inflow Mixing. *J. Atmos. Sci.* **2019**, *76*, 965–987. [CrossRef]
9. Blackwell, W.J.; Braun, S.; Bennartz, R.; Velden, C.; DeMaria, M.; Atlas, R.; Dunion, J.; Marks, F.; Rogers, R.; Annane, B.; et al. An overview of the TROPICS NASA Earth Venture Mission. *Q. J. R. Meteorol. Soc.* **2018**, *144*, 16–26. [CrossRef]
10. Sy, O.O.; Tanelli, S.; Durden, S.L.; Peral, E.; Sacco, G.-F.; Chahat, N.E.; Hristova-Veleva, S.; Heymsfield, A.J.; Bansemer, A.; Knosp, B.; et al. Scientific Products from the First Radar in a CubeSat (RainCube): Deconvolution, Cross-Validation, and Retrievals. *IEEE Trans. Geosci. Remote Sens.* **2021**, *60*, 1000320. [CrossRef]
11. Battaglia, A.; Kollias, P.; Dhillon, R.; Roy, R.; Tanelli, S.; Lamer, K.; Grecu, M.; Lebsock, M.; Watters, D.; Mroz, K.; et al. Spaceborne Cloud and Precipitation Radars: Status, Challenges, and Ways Forward. *Rev. Geophys.* **2020**, *58*, e2019RG000686. [CrossRef]

12. Stephens, G.; Freeman, A.; Richard, E.; Pilewskie, P.; Larkin, P.; Chew, C.; Tanelli, S.; Brown, S.; Posselt, D.; Peral, E. The Emerging Technological Revolution in Earth Observations. *Bull. Am. Meteorol. Soc.* **2020**, *101*, E274–E285. [CrossRef]
13. Stephens, G.L.; van den Heever, S.C.; Haddad, Z.S.; Posselt, D.J.; Storer, R.L.; Grant, L.D.; Sy, O.O.; Rao, T.N.; Tanelli, S.; Peral, E. A Distributed Small Satellite Approach for Measuring Convective Transports in the Earth's Atmosphere. *IEEE Trans. Geosci. Remote Sens.* **2020**, *58*, 4–13. [CrossRef]
14. Cardellach, E.; Oliveras, S.; Rius, A.; Tomás, S.; Ao, C.O.; Franklin, G.W.; Iijima, B.A.; Kuang, D.; Meehan, T.K.; Padullés, R.; et al. Sensing Heavy Precipitation with GNSS Polarimetric Radio Occultations. *Geophys. Res. Lett.* **2019**, *46*, 1024–1031. [CrossRef]
15. Padullés, R.; Ao, C.O.; Turk, F.J.; de la Torre Juárez, M.; Iijima, B.; Wang, K.N.; Cardellach, E. Calibration and validation of the Polarimetric Radio Occultation and Heavy Precipitation experiment aboard the PAZ satellite. *Atmos. Meas. Tech.* **2020**, *13*, 1299–1313. [CrossRef]
16. Wang, K.-N.; de la Torre Juárez, M.; Ao, C.O.; Xie, F. Correcting negatively biased refractivity below ducts in GNSS radio occultation: An optimal estimation approach towards improving planetary boundary layer (PBL) characterization. *Atmos. Meas. Tech.* **2017**, *10*, 4761–4776. [CrossRef]
17. Fitzgerald, R.; Halperin, L.; Leroy, S.; Gagnon, A.; Cahoy, K.; Clark, J. Analyzing Constellation Performance for the Radio Occultation Tomography of Internal Gravity Waves. *IEEE J. Sel. Top. Appl. Earth Obs. Remote Sens.* **2021**, *14*, 7225–7236. [CrossRef]
18. Cao, C.; Wang, W.; Lynch, E.; Bai, Y.; Ho, S.; Zhang, B. Simultaneous Radio Occultation for Intersatellite Comparison of Bending Angles toward More Accurate Atmospheric Sounding. *J. Atmos. Ocean. Technol.* **2020**, *37*, 2307–2320. [CrossRef]
19. Xu, X.; Han, Y.; Luo, J.; Wickert, J.; Asgarimehr, M. Seeking Optimal GNSS Radio Occultation Constellations Using Evolutionary Algorithms. *Remote Sens.* **2019**, *11*, 571. [CrossRef]
20. Tan, J.; Petersen, W.A.; Kirstetter, P.-E.; Tian, Y. Performance of IMERG as a Function of Spatiotemporal Scale. *J. Hydrometeorol.* **2016**, *18*, 307–319. [CrossRef]
21. Turk, F.J.; Padullés, R.; Ao, C.O.; de la Juarez, M.T.; Wang, K.-N.; Franklin, G.W.; Lowe, S.T.; Hristova-Veleva, S.M.; Fetzer, E.J.; Cardellach, E.; et al. Benefits of a Closely-Spaced Satellite Constellation of Atmospheric Polarimetric Radio Occultation Measurements. *Remote Sens.* **2019**, *11*, 2399. [CrossRef]
22. Shao, X.; Ho, S.; Zhang, B.; Cao, C.; Chen, Y. Consistency and Stability of SNPP ATMS Microwave Observations and COSMIC-2 Radio Occultation over Oceans. *Remote Sens.* **2021**, *13*, 3754. [CrossRef]
23. Iacovazzi, R.; Lin, L.; Sun, N.; Liu, Q. NOAA Operational Microwave Sounding Radiometer Data Quality Monitoring and Anomaly Assessment Using COSMIC GNSS Radio-Occultation Soundings. *Remote Sens.* **2020**, *12*, 828. [CrossRef]
24. Turk, F.J.; Padullés, R.; Cardellach, E.; Ao, C.O.; Wang, K.-N.; Morabito, D.D.; de la Juarez, M.T.; Oyola, M.; Hristova-Veleva, S.; Neelin, J.D. Interpretation of the Precipitation Structure Contained in Polarimetric Radio Occultation Profiles Using Passive Microwave Satellite Observations. *J. Atmos. Ocean. Technol.* **2021**, *38*, 1727–1745. [CrossRef]
25. Neelin, J.D.; Peters, O.; Hales, K. The transition to strong convection. *J. Atmos. Sci.* **2009**, *66*, 2367–2384. [CrossRef]
26. Kuo, Y.-H.; Schiro, K.A.; Neelin, J.D. Convective Transition Statistics over Tropical Oceans for Climate Model Diagnostics: Observational Baseline. *J. Atmos. Sci.* **2018**, *75*, 1553–1570. [CrossRef]
27. Eyring, V.; Bony, S.; Meehl, G.A.; Senior, C.A.; Stevens, B.; Stouffer, R.J.; Taylor, K.E. Overview of the Coupled Model Intercomparison Project Phase 6 (CMIP6) experimental design and organization. *Geosci. Model Dev.* **2016**, *9*, 1937–1958. [CrossRef]
28. Xie, S.; McCoy, R.B.; Klein, S.A.; Cederwall, R.T.; Wiscombe, W.J.; Jensen, M.P.; Johnson, K.L.; Clothiaux, E.E.; Gaustad, K.L.; Long, C.N.; et al. CLOUDS AND MORE: ARM Climate Modeling Best Estimate Data: A New Data Product for Climate Studies. *Bull. Am. Meteorol. Soc.* **2010**, *91*, 13–20. [CrossRef]
29. Emmenegger, T.; Kuo, H.Y.; Xie, S.; Zhang, C.; Tao, C.; Neelin, J.D. Evaluating Tropical Precipitation Relations in CMIP6 Models with ARM data. *J. Clim.* 2021; *in review*.
30. Holloway, C.E.; Neelin, J.D. Moisture Vertical Structure, Column Water Vapor, and Tropical Deep Convection. *J. Atmos. Sci.* **2009**, *66*, 1665–1683. [CrossRef]
31. Ahmed, F.; Neelin, J.D. Reverse engineering the tropical precipitation-buoyancy relationship. *J. Atmos. Sci.* **2018**, *75*, 1587–1608. [CrossRef]
32. Schiro, K.A.; Sullivan, S.C.; Kuo, Y.-H.; Su, H.; Gentine, P.; Elsaesser, G.S.; Jiang, J.H.; Neelin, J.D. Environmental Controls on Tropical Mesoscale Convective System Precipitation Intensity. *J. Atmos. Sci.* **2020**, *77*, 4233–4249. [CrossRef]
33. Romps, D.M. A Direct Measure of Entrainment. *J. Atmos. Sci.* **2010**, *67*, 1908–1927. [CrossRef]
34. Schiro, K.A.; Ahmed, F.; Giangrande, S.E.; Neelin, J.D. GoAmazon2014/5 campaign points to deep-inflow approach to deep convection across scales. *Proc. Natl. Acad. Sci. USA* **2018**, *115*, 4577–4582. [CrossRef]
35. Storer, R.L.; Posselt, D.J. Environmental impacts on the flux of mass through deep convection. *Q. J. R. Meteorol. Soc.* **2019**, *145*, 3832–3845. [CrossRef]
36. Ho, S.; Anthes, R.A.; Ao, C.O.; Healy, S.; Horanyi, A.; Hunt, D.; Mannucci, A.J.; Pedatella, N.; Randel, W.J.; Simmons, A.; et al. The COSMIC/FORMOSAT-3 Radio Occultation Mission after 12 Years: Accomplishments, Remaining Challenges, and Potential Impacts of COSMIC-2. *Bull. Am. Meteorol. Soc.* **2020**, *101*, E1107–E1136. [CrossRef]
37. Efron, B.; Tibshirani, R. Bootstrap Methods for Standard Errors, Confidence Intervals, and Other Measures of Statistical Accuracy. *Stat. Sci.* **1986**, *1*, 54–75. [CrossRef]

38. Cardellach, E.; Tomás, S.; Oliveras, S.; Padullés, R.; Rius, A.; de la Torre-Juárez, M.; Turk, F.J.; Ao, C.O.; Kursinski, E.R.; Schreiner, B. Sensitivity of PAZ LEO Polarimetric GNSS Radio-Occultation Experiment to Precipitation Events. *IEEE Trans. Geosci. Remote Sens.* **2014**, *53*, 190–206. [CrossRef]
39. Padullés, R.; Cardellach, E.; Turk, F.J.; Ao, C.O.; de la Torre Juárez, M.; Gong, J.; Wu, D.L. Sensing Horizontally Oriented Frozen Particles with Polarimetric Radio Occultations Aboard PAZ: Validation Using GMI Coincident Observations and Cloudsat a Priori Information. *IEEE Trans. Geosci. Remote Sens.* **2021**, *60*, 4101513. [CrossRef]
40. Fiolleau, T.; Roca, R. An algorithm for the detection and tracking of tropical mesoscale convective systems using infrared images from geostationary satellite. *IEEE Trans. Geosci. Remote Sens.* **2013**, *51*, 4302–4315. [CrossRef]
41. Hinson, D.P. Radio occultation measurements of transient eddies in the northern hemisphere of Mars. *J. Geophys. Res. Planets* **2006**, *111*, E05002. [CrossRef]
42. Johnston, B.R.; Randel, W.J.; Sjoberg, J.P. Evaluation of Tropospheric Moisture Characteristics Among COSMIC-2, ERA5 and MERRA-2 in the Tropics and Subtropics. *Remote Sens.* **2021**, *13*, 880. [CrossRef]
43. Ruston, B.; Healy, S. Forecast Impact of FORMOSAT-7/COSMIC-2 GNSS Radio Occultation Measurements. *Atmos. Sci. Lett.* **2019**, *22*, e1019. [CrossRef]
44. Maier, M.W.; Gallagher, F.W.; Germain, K.S.; Anthes, R.; Zuffada, C.; Menzies, R.; Piepmeier, J.; Pietro, D.D.; Coakley, M.M.; Adams, E. Architecting the Future of Weather Satellites. *Bull. Am. Meteorol. Soc.* **2021**, *102*, E589–E610. [CrossRef]